# Reaction kinetic acceleration induced by atomic-hybridized channels in carbon quantum dot/ReS$_2$ composites for efficient Cr(VI) reduction

Gang Zhou [a,1], Qifan Wu [c,1,*], Liqian Wu [b], Lizhe Liu [c,*], Dunhui Wang [b,c], Peifang Wang [a,**]

[a] Key Laboratory of Integrated Regulation and Resource Development on Shallow Lake of Ministry of Education, College of Environment, Hohai University, Nanjing 210098, China
[b] College of Electronics and Information, Hangzhou Dianzi University, Hangzhou 310018, China
[c] National Laboratory of Solid State Microstructures, Nanjing University, Nanjing 210093, China

ABSTRACT

The design of the excellent photocatalyst with high catalytic activity and light response characteristics remains a significant challenge for heavy metal reduction. Different from conventional heterostructures, this work focuses on a simple and feasible atomic-hybridized strategy to accelerate reaction kinetic process through constructing an electronic channel. Herein, we present an interesting molecule tailoring method to open C═O double bonds of carbon quantum dots (CQDs) and then anchor it onto ReS$_2$ nanosheets to form an electronic channel via Re-*5d* and O-*2p* orbital hybridization, in which photoinduced carrier of surface-reduced CQDs (rCQDs) can freely transfer to ReS$_2$ for hexavalent chromium reduction. Compared to pristine ReS$_2$ nanosheets and CQDs/ReS$_2$, the reduction reaction rate constant over the pseudo-first-order kinetic model is enhanced about 13.1 and 4.3 times, respectively. Our findings provide new inspirations for steering electronic channel by atomic hybridization and accelerating reaction kinetic mechanism simultaneously.

## 1. Introduction

Humankind has relied on utilization of heavy metals for thousands of years, causing significant degradation of global environment [1,2]. For example, the existence of Cr(VI) in aquatic system and drinking water sources can increase the threat of severe diarrhea and ladder, kidney, liver and skin canners, due to its acute toxicity to most of organism strong carcinogenic property and its high solubility in water [3]. Therefore, the removal of high toxic Cr(VI) from water to achieve World Health Organization (WHO) safety standard becomes a most urgent duty in life environment science. To solve this problem, huge efforts have been made to conduct wastewater treatment, such as adsorption [4,5], membrane filtration [6], chemical precipitation [7]. However, the most feasible method is the transformation of Cr(VI) to Cr(III) [8–10], because Cr(III) is lowly toxic and can be easily precipitated and removed as a solid waste like Cr(OH)$_3$ [11,12]. Photocatalytic Cr(VI) reduction is usually considered to be a promising and practical option because this method is more effective and low-cost, and does not produce any

hazardous chemicals [13–15]. A grand challenge is the lack of excellent photocatalysts with high light response and fast carrier tra0nsfer to drive efficient Cr(VI) reduction [16]. To obtain excellent catalytic performance, most research attentions have been directed toward preparing different composites, such as constructing various heterostructures [17–21], introducing vacancies or dopants [22–25].

It is generally known that a promising photocatalyst should possess high hole-electron pair separation (appropriate band structure) and large number of exposed superficial area [26–28]. These key elements strongly depend on the design of material's electronic structure [29–31]. In principle, the reaction kinetic acceleration should be considered from the regulation of electronic structure, such as atomic hybridization. If an electronic channel is constructed by atomic hybridization in a special heterostructure, the photoexcited carriers can efficiently transfer from one portion to another, leading to an expected reduction performance [32].

Herein, inspired by above considerations, we propose to synthesize a carbon quantum dots (CQDs)/ReS$_2$ heterostructure as a research model

---

to investigate how atomic hybridization forms an electronic channel to drive photoexcited carrier redistribution. Form material's viewpoint, our consideration is mainly based on the following aspects. Unlike other hexagonal two-dimensional (2D) transition-metal dichalcogenide semiconductors (TMDCSs) [33–35], layered $ReS_2$ crystallizes from the distorted diamond-chain structure with triclinic symmetry due to charge decoupling from an extra valence electron of the Re atom [36–38]. The distorted structure leads to much weaker interlayer coupling, and band renormalization is absent. Therefore, $ReS_2$ nanosheets behave as an electronically decoupled monolayer. The vanishing interlayer coupling is advantageous to exclude layer thickness contribution onto light response. In addition, CQDs have excellent light response characteristics and its superficial C═O bonds can be tailored more easily. As expected, in surface-reduced CQDs (rCQDs)/$ReS_2$ heterostructure, the strong electron-electron interaction induced by electronic hybridization between Re-*5d* and O-*2p* orbitals can lead to an electronic channel between rCQDs to $ReS_2$ nanosheets. The generation of this hybridized atomic configuration has an obvious advantage for transferring carriers to conduct reduction, thus eventually accelerating the reaction kinetic process.

## 2. Experimental section

### 2.1. Synthesis of $ReS_2$ nanosheets

$ReS_2$ nanosheets were grown on p-Si (resistivity1-5Ω·cm, B-doped, (100) orientation, 500 μm thickness) substrate by chemical vapor deposition (CVD) method. The p-Si substrate was placed above a quartz boat with 30 mg of $Re_2O_7$ powder and loaded into CVD furnace with the diameter of 3 cm. Another boat containing 700 mg Sulfur powder was located upstream wrapped with a resistance heater. The furnace was first purged with ultra-high purity Ar (99.999 %) for around 30 min and then CVD growth was performed at atmospheric pressure with flowing Ar at a rate of 20 sccm (standard cubic centimeters per minute). The temperature ramping rate was about $10\ ^{\circ}C\ min^{-1}$, and maintained at $750\ ^{\circ}C$ for 40 min. After the system was cooled down to room temperature under Ar gas environment, a layer of black product was obtained on the surface of p-Si substrate.

### 2.2. Synthesis of CQDs

Water-soluble, carboxyl-conjugated CQDs were synthesized via a solvothermal route by polymerization reaction of citric acid and urea. Typically, 1 g of citric acid and 2 g of urea were dissolved in 10 mL dimethylformamide (DMF) solvent. The mixed solution was transferred to a 25 ml polytetrafluoroethylene autoclave and reacted at 160 °C for 6 h. After the reactor cooled naturally to room temperature, the solution was transferred to a centrifuge tube and centrifuged at 9000 rpm for 15 min to remove large particles. And then the obtained dark-red suspension was further dialyzed through a dialysis membrane (MESH = 10,000) for 48 h to remove nonreacted ions and small particles. Finally, the above solution was mixed with ethanol (1:5) and centrifuged at 12,000 rpm for 10 min. The precipitate was collected, dispersed in deionized water, and centrifuged (16,000 rpm, 10 min) twice to wash off residual salts and alkali, and then freeze-dried to obtain the product of CQDs.

### 2.3. Synthesis of rCQDs

The dried CQDs were dissolved in 15 ml deionized water and then introduced with 0.15 g of sodium borohydride ($NaBH_4$). The homogeneous mixed solution was stirred at room temperature overnight under the protection of high-purity argon current. The obtained solution was treated in the same method as the described above to obtain the rCQDs sample.

### 2.4. Synthesis of rCQDs(CQDs)/ReS_2

A two-step hydrothermal process was adopted to anchor rCQDs or CQDs onto the surface of $ReS_2$ nanosheets. As a typical procedure, the as-prepared $ReS_2$ nanosheets array with Si substrate was immersed into the 2.5 g/L deionized water solution of rCQDs(CQDs) for ~30 min and then transferred together into a polytetrafluoroethylene autoclave. The reaction was carried out for 24 h at 65 °C. After naturally cooling to room temperature, the complex heterojunction on the substance was washed three times with deionized water and ethanol, respectively. As a result, we can remove the redundant rCQDs(CQDs) through this treatment.

### 2.5. Characterization

The morphology and microstructure of the samples were characterized by field emission scanning electron microscope (FE-SEM, Hitachi, S4800) equipped with Energy Dispersive X-Ray Spectroscopy (EDS) and high-resolution transmission electron microscope (HR-TEM, JEOL-2100). X-ray diffraction (XRD) measurements were conducted on the Shimadzu XRD-7000 diffractometer with Cu Kα radiation ($\lambda = 0.15406$ nm) to study the crystal structure. XPS measurements were carried out on an VG ESCALAB MKII using a monochromatic Al Ka x-ray beam. UV–vis-NIR absorption spectroscopic characterization was performed using a Cary 5000 spectrophotometer. FTIR was conducted on a Nicolet Nexus870 system using the standard KBr pellet technique. The PL and PLE spectra were acquired on an Edinburgh FLS-920 PL spectrometer.

### 2.6. Measurements of photocatalytic activity

The photocatalytic activity of the catalyst (1.5 cm*3 cm) was evaluated by visible-light photocatalytic reduction of Cr(VI). Cr(VI) stock solution (20 mg $L^{-1}$) was prepared by dissolving $K_2Cr_2O_7$ in distilled water. The photocatalyst was firstly placed in a 40 ml Cr(VI) solution and stirred in a dark room for 1 h to establish the entire catalytic system reaching an adsorption-desorption equilibrium between the catalyst and the pollutant. The mixed suspension under continuous stirring was exposed to light irradiation produced by a 300 W xenon lamp with an AM 1.5 filter. During the illumination process, about 2 mL of the aqueous solution was taken out at intervals of 10 min. The reduction process of Cr(VI) was monitored by UV–vis spectrophotometer at 352 nm absorption wavelength. After the reaction, the catalyst was washed repeatedly with deionized water and anhydrous ethanol for three times and dried in vacuum environment for 24 h.

### 2.7. Calculation methods

The photonic efficiency ξ, which is defined as the ratio of the dye reduction rate and the incident photon flux, is calculated according to equation [39]:

$$\xi = \frac{degradation\ rate\ [mol \cdot s^{-1}]}{photon\ flux\ [mol \cdot \nu \cdot s^{-1}]} = \frac{\Delta C \cdot V}{\Delta t \cdot I_0 \cdot S}$$

$$I_0 = \frac{I \cdot \lambda}{N_A \cdot h \cdot c}$$

So,

$$\xi = \frac{\Delta C \cdot V}{\Delta t} \cdot \frac{N_A \cdot h \cdot c}{I \cdot \lambda \cdot S}$$

Where $\Delta C / \Delta t$ is the reduction rate, V is the volume of the employed test solution, $I_0$ is the photo flux, S is the illuminated area, I is the total light intensity, $\lambda$ is incident wavelength, $N_A$ is the Avogadro's constant, *h* is the Planck's constant and c is the velocity of light.

## 2.8. DFT calculation

The theoretical assessment is based on the density-functional theory in Perdew-Burke-Ernzerhof (PBE) generalized gradient approximation (GGA) using the Vienna *ab inito* simulation package (VASP) code with projector augmented wave pseudopotentials [40,41]. The plane-wave energy cutoff of 460 eV is used to expand the Kohn-Sham wave functions and relaxation is carried out until all forces on the free ions converge to 0.01 eV/Å. The vacuum space is at least 20 Å, which is large enough to avoid the interaction between periodical images. The Monkhorst-Pack *k*-points grid is $6 \times 6 \times 1$, which has been tested to be well converged.

## 3. Results and discussion

### 3.1. Characterization of carbon quantum dots

Based on previous experimental reports [42–44], the main synthesis strategy of our designed sample is schematically shown in Fig. 1. Firstly, the $ReS_2$ nanosheets with three-dimensional porous textures are assembled onto a p-Si substrate by chemical vapor deposition (CVD) method. Simultaneously, the CQDs was synthesized by solvothermal procedure with citric acid and urea as the source, respectively. It is generally known that the surface of CQDs is usually covered by C=O bonds, which has obvious disadvantage in anchoring onto $ReS_2$ nanosheet [45]. To overcome this difficulty, $NaBH_4$ solution is added into the above homogeneous CQDs solution to turn C=O bonds into CH—OH configuration, named as rCQDs sample. Subsequently, the highly reactive CH—OH functional groups can hybridize with $ReS_2$ surface more easily through a simple second hydrothermal process. As expected, our proposed rCQDs/$ReS_2$ composites can be obtained by this synthetic route.

According to the aforementioned composite strategy, the rCQDs are fabricated to discuss its electronic structure. Fig. 2a depicts the TEM image of the synthesized rCQDs, which are almost spherical structure due to the surface-free energy minimization. The size distribution discloses that the diameters of the rCQDs are between 4.5 and 5.0 nm (Fig. S1). The left inset in Fig. 2a exhibits the high-resolution TEM image of one representative rCQD with a lattice fringe spacing of 0.32 nm, which corresponds to the (002) plane of graphite [46]. In order to disclose the superficial modification, the Fourier Transform Infrared Spectra (FT-IR) of CQDs and rCQDs are shown in Fig. 2b as a comparison. We can see that the synthesized CQDs contain rich surface groups, such as carbonyl C=O, carboxy COOH, hydroxyl C—OH, and amino groups. After CQDs are treated by $NaBH_4$, the FT-IR spectrum of rCQDs disclose that the C=O tensile vibrational absorption peak corresponding to 1674 cm$^{-1}$ is almost quenched. Compared to that of CQDs [47], the absorption band at 3000−3600 cm$^{-1}$ from the surface hydroxyl groups stretching vibration is increased. At the same time, the absorption band at 869−1003 cm$^{-1}$ from O—H vibration also be enhanced. The corresponding evolutions from C=O to C—OH and O—H signals indicate the reduction from carbonyl to hydroxyl groups. The C 1s core-level X-ray photoelectron spectra (XPS) spectra acquired from the rCQDs is shown in the Fig. 2c. The strongest peak at 284.6 eV can be attributed to the conjugated sp$^2$ C=C/C—C component, and two weak peaks on the high-energy side at 288.0 eV and 288.9 eV correspond to the C—N group and C=O group [48]. It is important to note that the XPS peak originated from C—OH group at 286.2 eV can be observed, which is obviously enhanced compared to that of CQDs (Fig. S2). The XPS and FTIR spectra undoubtedly disclose that the C=O bonds of CQDs turn into C—OH group through $NaBH_4$ treatment.

To better understand the contribution of C=O bond switch, the charge density difference, defined as $\Delta\rho = \rho_{CQD} - \rho_O$, is calculated and shown in Fig. 2d. Here, $\rho_O$ represent the charge density of C=O covering on CQD surface, $\rho_{CQD}$ is the charge density of CQD. The yellow isosurface corresponds to an electron depletion zone, while the blue one is an electron increase zone. When C=O is formed onto CQD surface, the orbital hybridization makes electronic wave functions are redistributed. Therefore, the electron depletion zone and electron increase zone are mainly located at superficial C and O atoms. When the C=O group is modified into C—OH configuration, as shown in Fig. 2e, the existence of H* will inject additional electrons into C=O bond and then occupies the *p* orbital of O atom. As a result, the atomic hybridization at C=O is depressed and the electron depletion zone of C atoms is reduced correspondingly. The Bader charge analysis about C atom disclose that it is increased into 10.05 e (C—OH) from 8.75 e (C=O), which indicates that electronic wave overlapping between C and O is suppressed. The orbital-resolved total density of state (DOS) is displayed in Fig. 2f. Compared to DOS of CQD, the *p* orbitals of C atom in rCQD are red-shifted to the Femi energy, leading to high reaction activity. Therefore, more electrons at valence band can be transferred and hybridized to form composites. In addition, the px orbital play a dominating role in DOS distribution and its intensity of py orbital is also enhanced in rCQD. The charge and DOS difference between CQD and rCQD reveal that the structural transformation from C=O to C—OH can lead to a feasible atomic hybridization with $ReS_2$ nanosheets.

### 3.2. Electronic structure of carbon quantum dots

Spectroscopic characterization is a useful tool to identify microstructural changes and relative electronic structures [49–53]. To disclose the changes in electronic structure, Fig. 3a shows the photoluminescence (PL) spectra acquired from the CQDs in different electron sacrificial agent (ES, $K_2S_2O_8$) concentration excited by the 320 nm line of a xenon lamp. Without adding ES (0 M), a typical double-peak feature occurs at 465 nm and 520 nm, which has been assigned to π-π* transition of sp$^2$ domains and existence of C=O bonds. Interestingly, the PL peak originated from π-π* transition sharply decreases as increasing ES concentration due to stronger consumption of photogenerated electrons, however the PL peaks relative with C=O bonds keep nearly constant.
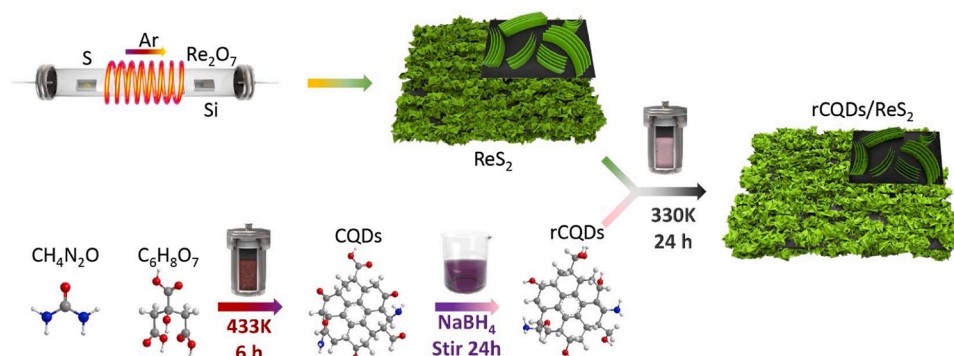
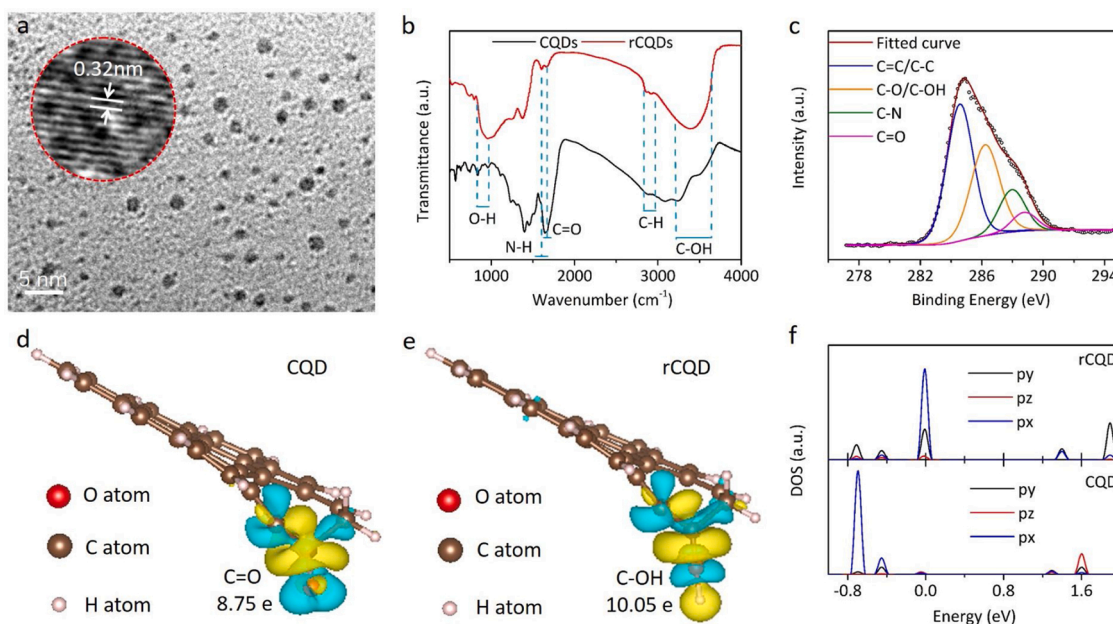**Fig. 1.** Schematic illustration of the preparation process.

**Fig. 2. a**, The TEM image of rCQDs. Inset: The HR-TEM image of rCQD. **b**, The FT-IR spectrum of CQDs and rCQDs. **c**, The C 1s core-level XPS spectra of rCQDs. **d**, The charge density difference of CQD. **e**, The charge density difference of rCQD. **f**, The orbital-resolved DOS of CQD and rCQD.
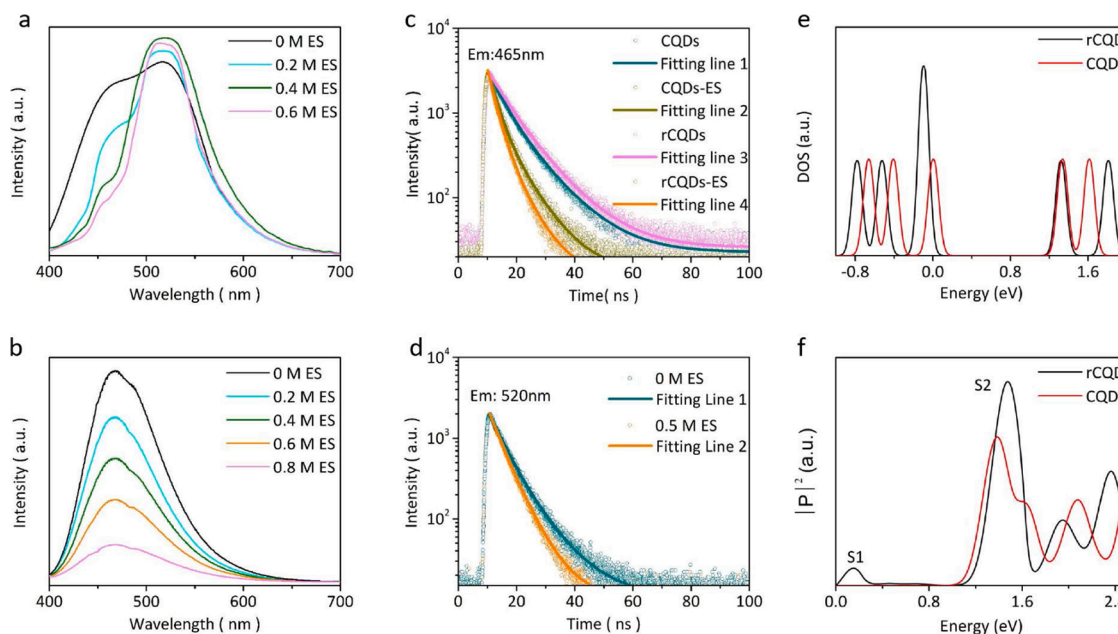


**Fig. 3.** PL spectra (375 nm excitation) of **a**, CQDs and **b**, rCQDs in aqueous solutions with the varying concentrations of electronic sacrificial agent (ES, $K_2S_2O_8$). **c**, Time-resolved emission spectra (TRES) of CQDs and rCQDs in aqueous solutions with the varying concentrations of ES. The 465 nm PL decay line is detected under excitation by the 375 nm lines. **d**, TRES of CQDs in aqueous solutions with the varying concentrations of ES. The 520 nm PL decay line is detected under excitation by the 375 nm lines. **e**, Total DOS of CQDs and rCQDs. **f**, Optical transition matrix element associated with CQD and rCQD.

This result indicates that photoexcited carriers prefer to localization at superficial C=O bonds, in which the carrier kinetic process at C=O bonds cannot be affected by ES introduction. When the C=O bonds are modified as C—OH structure, as shown in Fig. 3b, the PL peaks are slightly red-shifted and it intensity decreases obviously with ES concentration increases. This PL behavior dependent of adding ES implies that rCQDs with superficial C—OH configuration will conduce to an electronic hybridization (Fig. S3). Notably, it can be believed that the unique rCQDs can serve as both solar photon harvester and photoinduced charge generator.

In order to disclose the carrier dynamic process, as shown in Fig. 3c

and d, the 465 and 520 nm PL decay lines are detected under excitation by the 375 nm lines, respectively. The emission decay line can be fitted by a biexponential function, $\Delta R/R_0(t) = A_1 \exp(-t/\tau_1) + A_2 \exp(-t/\tau_2)$, where the parameters $\tau_1$ and $\tau_2$ is the carrier lifetime. For 465 nm emission in Fig. 3c, the carrier lifetime $\tau_1$ and $\tau_2$ for CQD is shorten to 2.78 ns ($\tau_1$) and 7.80 ns ($\tau_2$) in 0.5 M ES from 4.78 ns ($\tau_1$) and 11.12 ns ($\tau_2$) in water. And the lifetime component contributes to 40.21 % ($\tau_1$) and 59.79 % ($\tau_2$) of the total signal in water and 47.72 % ($\tau_1$) and 52.28 % ($\tau_2$) in 0.5 M ES, respectively. However, the rCQDs show an obvious different dynamic process. In water, the carrier lifetime $\tau_1 = 6.07$ ns and $\tau_2 = 11.53$ ns and the corresponding component is 40.92 % and 59.08

%. When 0.5 M ES is added into water solution, the carrier lifetime is reduced as $\tau_1 = 2.70$ ns and $\tau_2 = 6.67$ ns and the corresponding component becomes 61.25 % and 38.75 %. In order to give a better comparison between CQD and rCQD, the emission decay average lifetime can be considered as: $\tau = \sum_{i=1}^{i=2} A_i \tau_i^2 / \sum_{i=1}^{i=2} A_i \tau_i$. For CQD sample, the introduction of ES for rCQDs make its average lifetime $\tau$ decrease to 6.67 ns from 11.53 ns, which is more obvious shorten than that of CQDs from 7.88 ns to 11.12 ns. The shorten lifetime furthermore discloses that large number of photo-excited carriers on rCQDs overflowing toward solution can be quickly captured by the electron sacrificial agent due to the existence of C—OH group. As another evidence, the 520 nm emission decays of CQDs is provided in Fig. 3d, in which average lifetime is $\tau = 7.96$ ns in water, $\tau = 6.31$ ns in 0.5 M ES. This slight lifetime change displays that CQD surface coved by C═O bonds is hardly affected by charging effect. On the contrary, rCQDs with modifying C—OH bonds exhibit a better hybridized activity.

To theoretically elucidate the dependence of the electronic structure on the superficial modification, the total density of state (DOS) of one CQD and rCQD is calculated and shown in Fig. 3e. Compared to the result of CQD, the DOS intensity of rCQD at valence band maximum (VBM) is enhanced about 2 times but the intensity at conduction band minimum (CBM) keeps unchanged hardly. The electronic state difference between VBM and CBM implies that more valence electrons can join into optical transition and orbital reconfiguration. Therefore, the PL intensity of rCQDs can be depressed due to the interaction between C—OH and ES. For a CQD, the DOS intensity at CBM and CBM are equal and the orbitals at CBM can fully accommodate photo-excited carrier. As a result, the interaction between C═O and ES can be neglected, leading to a stable emission at 520 nm in different ES concentration. Based on above analysis, the specific contribution of the surface with C═O and C—OH structures to electron-hole recombination can be investigated by computing the optical transition matrix element associated with CQD and rCQD, which is defined as [54]

$$|P|^2(E) = \sum_{\rightarrow_k}, v, c \left| \left\langle \psi_{\rightarrow_k}^c \left(\rightarrow_r\right) \middle| \rightarrow_u \cdot \rightarrow_r \middle| \psi_{\rightarrow_k}^v \left(\rightarrow_r\right) \right\rangle \right|^2 \delta(E_{\rightarrow_k}^c - E_{\rightarrow_k}^v - E),$$

where E is the transition energy, $\rightarrow_k$ is the Bloch wave vector of the superlattice, $E_{\rightarrow_k}^{c(v)}$ and $|\psi_{\rightarrow_k}^v \left(\rightarrow_r\right)\rangle$ are the eigen-energy and wave func-

tion of the state in the conduction (valence) band, respectively, $\rightarrow_r$ is the position vector, and $\rightarrow_u$ is the unit vector along the polarization of the light. As a general tendency in Fig. 3f, the $|P|^2$ peak (marked by S2) is enhanced and blue-shifted from C═O to C—OH configuration. It is consistent with the above DOS results and PL measurement. In addition, a small peak (marked as S1) can be clearly observed for C—OH configuration due to the orbital hybridization between C and O atoms. The trend of $|P|^2$ modification (electronic transitions between valence and conduction bands) with different superficial modification display a good reaction activity for rCQD. As expected, the atomic hybridization between rCQD to ReS₂ to form electronic channels is feasible strategy.

### 3.3. Characterization of carbon quantum dots/ReS₂ heterojunctions

Through further hydrothermal synthesis, the rCQDs are assembled onto ReS₂ surface to fabricate expected heterostructures. The scanning electron microscopy (SEM) image in Fig. 4a disclose that the rCQDs /ReS₂ nanosheets were vertically aligned onto the Si substrate with three-dimensional porous textures. Those nanosheets are observed to be well-organized and connected with each other to form a stereoscopic structure with a large faction of exposed edges and patulous pores. The transmission electron microscopy (TEM) image of the nanosheets exfoliated from Si substrate as shown in Fig. S4 disclose that the size of each nanosheet is about 350 ~ 500 nm. This special porous morphology has an obvious advantageous in harvesting solar energy [55,56]. The high-resolution TEM (HR-TEM) image in Fig. 4b reveals that two different lattice orientations with a resolved 0.32 nm and 0.61 nm can be observed, which corresponds to the graphite (002) and ReS₂ (001) planes. Noting that the decorating with CQDs into ReS₂ nanosheets, the dense alignment of vertical oriented nanosheets remains almost unchanged, as shown in Fig. S5. This result discloses that rCQDs have been successfully assembled onto ReS₂ nanosheet, fabricating a rCQDs/ReS₂ heterostructure. Specific surface areas of different samples are evaluated by nitrogen adsorption–desorption curves, as shown in Fig. S6. The specific surface areas are 96.29 m²/g and 98.11 m²/g for ReS₂ and rCQDs/ReS₂, respectively. From this conclusion, it can be seen that the anchoring of rCQDs hardly change the surface areas of pristine ReS₂. Additionally, the X-ray diffraction (XRD) pattern in Fig. 4c is
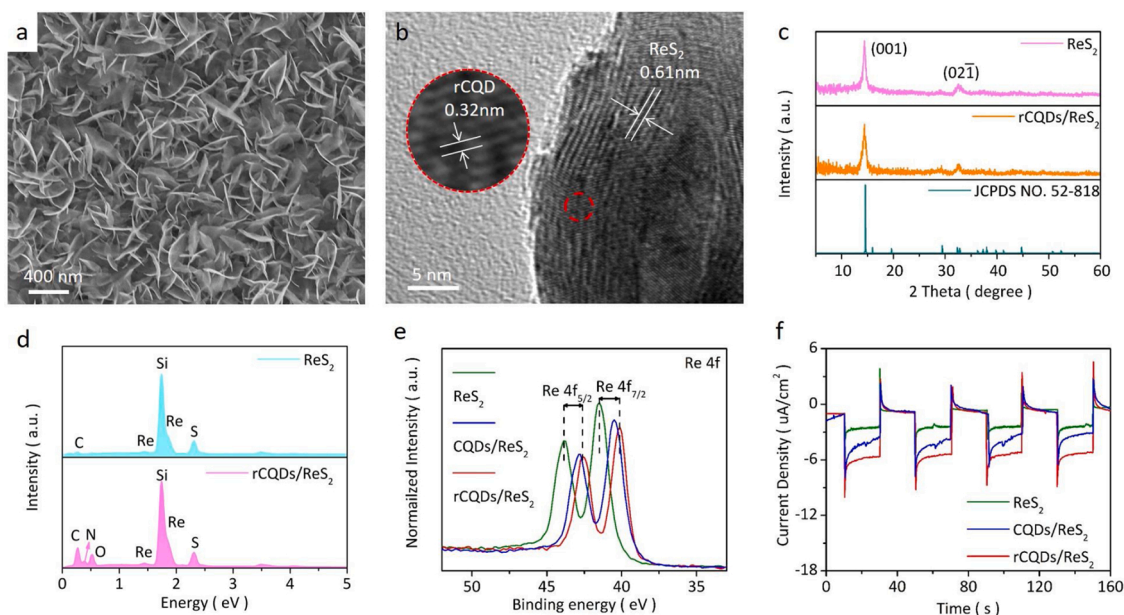


**Fig. 4.** Characterization of carbon quantum dots/ReS₂ heterojunctions. **a,** The SEM image of rCQDs/ReS₂ heterojunctions. **b,** The HR-TEM image of rCQDs/ReS₂ heterojunctions. Inset: The corresponding TEM image. **c,** The XRD pattern and **d,** the EDS spectra of ReS₂ nanosheets and rCQDs/ReS₂ heterojunctions. **e,** High-resolution Re 4f XPS spectra of the as-prepared rCQDs(CQDs)/ReS₂ heterojunctions and ReS₂ nanosheets. **f,** The photocurrent transient response of as-prepared rCQDs(CQDs)/ReS₂ heterojunctions and ReS₂ nanosheets in 0.1 M Na₂SO₄ aqueous solution under UV–vis light irradiation.

undoubtedly identical to formation of ReS$_2$, which is consistent with that of JCPDS Card (No. 52-818). After forming rCQDs/ReS$_2$ composites, no other discernible peaks appear with introducing rCQDs, showing that expected rCQDs cannot change the original ReS$_2$ crystal structure. The energy-dispersive X-ray spectrum (EDS) in Fig. 4d provide clear visual evidence that C, S, and Re elements are homogenously distributed in the surface of rCQDs/ReS$_2$ composite, suggesting that rCQDs are uniformly implanted into the parent ReS$_2$ nanosheets.

As another evidence, the high-resolution XPS spectra in Re 4f and S 2p regions, as shown in Fig. 4e and Fig. S7, identify the dominant peaks of Re 4f$_{5/2}$, Re 4f$_{7/2}$, S 2p$_{1/2}$, and S 2p$_{3/2}$. In pristine ReS$_2$ sample, the f shell of Re atoms splits into two symmetric peaks of 4f$_{7/2}$ and 4f$_{5/2}$ at 41.51 and 43.86 eV, respectively, indicating Re as metal species with no inherent oxide. Noticeably when hybridized with CQDs or rCQDs, these characteristic peaks from Re 4f shift toward lower binding energies, indicating a strong electronic interaction between ReS$_2$ and CQDs/ rCQDs. Interestingly, the XPS peak shifts in rCQDs/ReS$_2$ is more obvious (~ 1.3 eV) than that of CQDs/ReS$_2$ (~1.0 eV), because charge electrons of rCQDs can transfer to ReS$_2$ more easily. It is generally known that charge localization can be destroyed by reduction of C=O bonds, leading to a stronger orbital hybridization [34]. Therefore, we deduce that electronic channels are formed in rCQDs/ReS$_2$ composites through atomic hybridized strategy. To better display the advantages of electronic channels, the I-t curves under the chopped-light illumination are provided in Fig. 4f. Compared to pure ReS$_2$, the photocurrent is enhanced about 1.5 times (CQDs/ReS$_2$) and 2.0 times (rCQDs/ReS$_2$), which can be attributed to high light response of carbon dots and formation of electronic channels. Notably, the atomic hybridization in rCQDs/ReS$_2$ has more obvious advantage for carrier transfer, indicating its stronger abilities of hot electron generation and output. In order to confirm the difference in heterojunctions, the zeta potentials of ReS$_2$ nanosheets, rCQDs and rCQDs/ReS$_2$ were examined and shown in Table S1. The zeta potentials were -31.7 mV, -5.3 mV and −33.4 mV for ReS$_2$ nanosheets, rCQDs and rCQDs/ReS$_2$, respectively. The negative zeta potentials indicate that a large number of negative charges appear at rCQDs/ReS$_2$ surface in DI water, leading to an excellent Cr(VI) reduction performance.

### 3.4. Reduction performance and mechanism

To demonstrate the contribution of electronic channels, Fig. 5a show the time-dependent reduction curves of Cr(VI) with ReS$_2$ nanosheets, CQDs/ReS$_2$, rCQDs/ReS$_2$ and blank under 300 W xenon lamp irradiation for 50 min. The adsorption-desorption process is shown in Fig. S8. Herein, C$_0$ and C is the initial and actual concentration after the adsorption–desorption equilibrium, the reduction efficiency (η) can be expressed as $\eta\ (\%)= (1-C/C_0)*100$. In the absence of photocatalysts, the Cr(VI) concentration keep unchanged under light irradiation, showing none self-degradability. When rCQDs/ReS$_2$ composites are added, Cr (VI) is almost completely degraded within 50 min, with a reduction rate η of 95.6 %. This performance is obviously better than that of ReS$_2$ (η = 20.7 %) and CQDs/ReS$_2$ (η = 51.5 %). In the photocatalytic reaction, the influence of p-Si substrate onto rCQDs/ReS$_2$ heterojunctions can be neglected (Fig. S9). Compared with some standard photocatalyst, rCQDs/ReS$_2$ shows more excellent photocatalytic activity (Fig. S10 and Table S2). The effect of pH value on the photocatalytic reduction of Cr (VI) for rCQDs/ReS$_2$ was also discussed in Fig. S11. In order to quantitatively evaluate the photocatalytic activity of these catalysts, based on pseudo first-order kinetic model, the equation $ln(C_0/C)=kt$ was used to evaluate the reduction rate, where $k$ is the apparent reaction rate constant. As shown in Fig. 5b, the reduction rate of ReS$_2$ to reduce Cr(VI) is only $4.68*10^{-3}$ min$^{-1}$, which is lower than CQDs/ReS$_2$ ($1.40*10^{-2}$ min$^{-1}$). The highest photocatalytic activity occurs at rCQDs/ReS$_2$, with a reduction rate of $6.39*10^{-2}$ min$^{-1}$, which can be attributed to the accelerated reaction kinetic induced by electronic channels. The first-order reaction rate constant, $k$ (min$^{-1}$), were determined for each pH by least-squares regression, and the results are shown in Fig. S12. It was observed that the reaction rate constant decreases linearly with an increase of pH value. The structural stability is another important parameter to evaluate the reduction performance. Therefore, the stability of rCQDs/ReS$_2$ sample was also experimentally tested and shown in Fig. 5c. No significant change in the photocatalytic efficiency takes place even after six photocatalytic cycle, indicating the rCQDs/ReS$_2$ can keep stable recyclability in acting as the pollutant photocatalyst. This structural stability is further confirmed by EDS, SEM and the photon efficiency (ξ) for the recycled rCQDs/ReS$_2$ after six cycles. As shown in Fig. S13 and Fig. S14 (see the Supporting Information), no noticeable
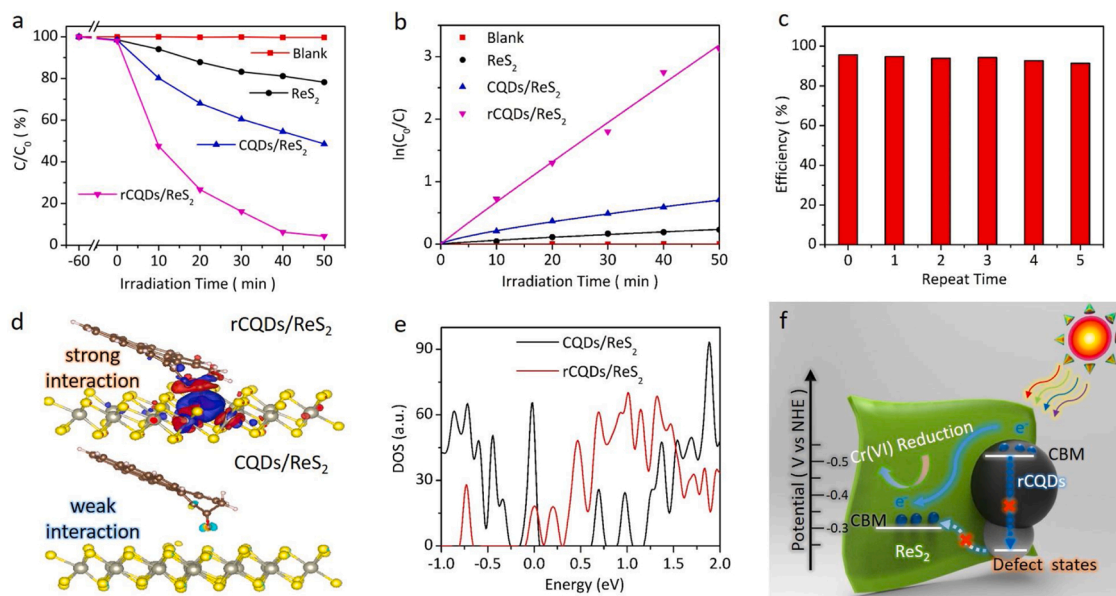


**Fig. 5. a**, Reduction curves of the Cr(VI) aqueous solutions containing different photocatalysts under simulated sunlight irradiation: no catalyst, ReS$_2$ nanosheets, CQDs/ReS$_2$ heterojunctions, and rCQDs/ReS$_2$ heterojunctions. **b**, The corresponding kinetic linear fitting curves of Cr(VI) reduction. **c**, The repetitive runs of the photoreduction of Cr(VI) in the presence of rCQDs/ReS$_2$ heterojunctions. **d**, The charge density difference of rCQD(CQD)/ReS$_2$ heterojunctions. **e**, The total DOS of CQD/ReS$_2$ and rCQD/ReS$_2$. **f**, Schematic presentation of the carrier transfer process in the rCQD(CQD)/ReS$_2$ heterostructure during reduction.

changes occur both in the EDS pattern and in the porous layered morphology before and after the photocatalytic process. And the photon efficiency ξ of the rCQDs/ReS₂ is 0.0287 %, 0.0285 %, 0.0281 %, 0.0283 %, 0.0278 % and 0.0274 % for the six cycles, showing an insignificant recession. The effects of the above charges on the catalytic process were discussed separately. In order to confirm the carrier separation mechanism, the photoreduction activities of rCQDs/ReS₂ in different scavengers are discussed in Fig. S15. In addition, the changed valence state of Cr was confirmed by XPS analysis (Fig. S16).

In order to understand the contribution of electronic channel, the charge density differences are calculated and shown in Fig. 5d. When the C=O bond is opened and hybridized with ReS₂, the electronic channel is formed as a bridge to transfer carrier conveniently (rCQDs/ReS₂, as shown in top panel). For CQDs/ReS₂ system in the bottom panel, the charge electrons are strongly localized around C=O bonds and the hybridized interaction between ReS₂ and CQD becomes weak. The difference in electronic channel can be used to explain the change in reduction rate. To clearly illustrate atomic hybridization, the total DOSs of rCQD/ReS₂ and CQD/ReS₂ are shown in Fig. 5e. The detailed electronic structure analysis shows that DOSs of rCQD/ReS₂ (marked by red) cross the Femi energy, whereas the CQD/ReS₂ ones show an obvious band gap. The atomic hybridization between rCQD and ReS₂ makes this system exhibits a good metallicity. Therefore, the carrier can be efficiently transported in rCQD/ReS₂ system and the reaction kinetic is accelerated via hybridized metal states. Finally, Fig. 5f depicts the schematic presentation of the carrier transfer process in the rCQD/ReS₂ heterostructure. Based on the Kubelka–Munk converted reflectance spectra (Fig. S17, S18), the optical band gap of ReS₂ nanosheets and rCQDs were obtained as 1.54 eV and 2.78 eV, respectively. The position of the energy level relative to the NHE can be determined by $E_{NHE}(V) = \Phi + E_{VL}(eV) - 4.44$, where E is the potential of normal hydrogen electrode; Φ is the electron work function of the analyzer (4.30 eV), $E_{VL}$ is the potential of vacuum level (Fig. S19) [57]. Therefore, the position of the conduction band of each component is -0.52 eV and -0.3 eV corresponding to rCQDs and ReS₂, respectively. As expected, a large amount of photo-generated carriers generated by rCQDs will be transferred into ReS₂ nanosheets through hybridized channels. As a result, the accumulated electrons on ReS₂ surface can be used to reduce Cr(VI) concentration. In CQDs/ReS₂ system, the photo-excited carriers prefer to be localized at surface of CQDs due to the lower C=O energy level, which not benefits for carrier transfer. This energy diagram demonstrates clearly the reaction kinetic process.

## 4. Conclusion

In summary, we have demonstrated that the atomic hybridization in rCQD/ReS₂ composites could provide an electronic channel to accelerate reaction kinetic process. The switch of C=O bonds not only benefits for atomic hybridization but also obviously facilitates carrier transfer, leading to an excellent reduction efficiency. Our work offers a new insight for accelerating reaction kinetic process in the fields of designing new-type photocatalysts, and may help to solve problems in heavy metal pollution. In view of the great variety of candidate materials, novel strategies from atomic hybridization could be foreseen to tune the catalytic reaction process.

## Declaration of Competing Interest

The authors declare that they have no known competing financial interests or personal relationships that could have appeared to influence the work reported in this paper.

## Acknowledgements

## Appendix A. Supplementary data

Supplementary data associated with this article can be found, in the online version, at https://doi.org/10.1016/j.apcatb.2020.119807.

## References

[1] A.S. Ellis, M.J. Thomas, D.B. Thomas, Chromium isotopes and the fate of hexavalent chromium in the environment, Science 295 (2002) 2060–2062, https://doi.org/10.1126/science.1068368.

[2] N. Yoshida, A.A. Tsaturyan, T. Akitsu, Y. Tsunoda, I.N. Shcherbakov, Photo-induced reduction of Cr⁶⁺ by the hybrid systems "Cu$^{II}$ complex with Schiff base and TiO₂": dependence on irradiation wavelength, Russ. Chem. Bull. 66 (2017) 2057–2065, https://doi.org/10.1007/s11172-017-1981-7.

[3] A.H. Smith, C.M. Steinmaus, Health effects of arsenic and chromium in drinking water: recent human findings, Annu. Rev. Public Health 30 (2009) 107–122, https://doi.org/10.1146/annurev.publhealth.031308.100143.

[4] D. Mohan, C.U. Pittman Jr, Activated carbons and low cost adsorbents for remediation of tri-and hexavalent chromium from water, J. Hazard. Mater. 137 (2006) 762–811, https://doi.org/10.1016/j.jhazmat.2006.06.060.

[5] J. Lee, H.G. Kim, J.H. Lee, S.H. Cho, K.W. Jung, S.Y. Lee, J.W. Choi, Performance differences of hexavalent chromium adsorbents caused by graphene oxide drying process, Sci. Rep. 10 (2020) 1–8, https://doi.org/10.1038/s41598-020-61760-2.

[6] J. Yoon, G. Amy, J. Chung, J. Sohn, Y. Yoon, Removal of toxic ions (chromate, arsenate, and perchlorate) using reverse osmosis, nanofiltration, and ultrafiltration membranes, Chemosphere 77 (2009) 228–235, https://doi.org/10.1016/j.chemosphere.2009.07.028.

[7] T.A. Kurniawan, G.Y. Chan, W.H. Lo, S. Babel, Physico–chemical treatment techniques for wastewater laden with heavy metals, Chem. Eng. J. 118 (2006) 83–98, https://doi.org/10.1016/j.cej.2006.01.015.

[8] C.L. Hsu, S.L. Wang, Y.M. Tzou, Photocatalytic reduction of Cr(VI) in the presence of NO₃⁻ and Cl⁻ electrolytes as influenced by Fe(III), Environ. Sci. Technol. 41 (2007) 7907–7914, https://doi.org/10.1021/es0718164.

[9] H. Wang, X. Yuan, Y. Wu, G. Zeng, X. Chen, L. Leng, Z. Wu, L. Jiang, H. Li, Facile synthesis of amino-functionalized titanium metal-organic frameworks and their superior visible-light photocatalytic activity for Cr(VI) reduction, J. Hazard. Mater. 286 (2015) 187–194, https://doi.org/10.1016/j.jhazmat.2014.11.039.

[10] F. Pinakidou, M. Katsikini, K. Simeonidis, E. Paloura, E.C. Kaprara, M. Mitrakas, On the passivation mechanism of Fe₃O₄ nanoparticles during Cr(VI) removal from water: a XAFS study, Appl. Surf. Sci. 360 (2016) 1080–1086, https://doi.org/10.1016/j.apsusc.2015.11.063.

[11] J. Qu, D. Chen, N. Li, Q. Xu, H. Li, J. He, J. Lu, Coral-inspired nanoscale design of porous SnS₂ for photocatalytic reduction and removal of aqueous Cr(VI), Appl. Catal. B: Environ. 207 (2017) 404–411, https://doi.org/10.1016/j.apcatb.2017.02.050.

[12] B. Saha, C. Orvig, Biosorbents for hexavalent chromium elimination from industrial and municipal effluents, Coord. Chem. Rev. 254 (2010) 2959–2972, https://doi.org/10.1016/j.ccr.2010.06.005.

[13] Y. Ku, I.L. Jung, Photocatalytic reduction of Cr(VI) in aqueous solutions by UV irradiation with the presence of titanium dioxide, Water Res. 35 (2001) 135–142, https://doi.org/10.1016/S0043-1354(00)00098-1.

[14] G. Jiang, Z. Lin, C. Chen, L. Zhu, Q. Chang, N. Wang, W. Wei, H. Tang, TiO₂ nanoparticles assembled on graphene oxide nanosheets with high photocatalytic activity for removal of pollutants, Carbon 49 (2011) 2693–2701, https://doi.org/10.1016/j.carbon.2011.02.059.

[15] L.B. Khalil, W.E. Mourad, M.W. Rophael, Photocatalytic reduction of environmental pollutant Cr(VI) over some semiconductors under UV/visible light illumination, Appl. Catal. B: Environ. 17 (1998) 267–273, https://doi.org/10.1016/S0926-3373(98)00020-4.

[16] C.E. Barrera-Díaz, V. Lugo-Lugo, B. Bilyeu, A review of chemical, electrochemical and biological methods for aqueous Cr(VI) reduction, J. Hazard. Mater. 223 (2012) 1–12, https://doi.org/10.1016/j.jhazmat.2012.04.054.

[17] G. Zhou, L. Long, P. Wang, Y. Hu, Q. Zhang, C. Liu, Designing CuO/ZnO nanoforest device toward optimal photocatalytic performance through structure and facet engineering, Mater. Lett. 273 (2020), https://doi.org/10.1016/j.matlet.2020.127907, 127907.

[18] J. Tian, Y. Sang, G. Yu, H. Jiang, X. Mu, H. Liu, A Bi₂WO₆ based hybrid photocatalyst with broad spectrum photocatalytic properties under UV, visible, and near infrared irradiation, Adv. Mater. 25 (2013) 5075–5080, https://doi.org/10.1002/adma.201302014.

[19] Y. Guo, Y. Ao, P. Wang, C. Wang, Mediator-free direct dual-Z-scheme Bi₂S₃/BiVO₄/MgIn₂S₄ composite photocatalysts with enhanced visible-light-driven performance towards carbamazepine degradation, Appl. Catal. B: Environ. 254 (2019) 479–490, https://doi.org/10.1016/j.apcatb.2019.04.031.

[20] G. Zhou, X. Xu, J. Yu, B. Feng, Y. Zhang, J. Hu, Y. Zhou, Vertically aligned MoS$_2$/MoO$_x$ heterojunction nanosheets for enhanced visible-light photocatalytic activity and photostability, CrystEngComm 16 (2014) 9025–9032, https://doi.org/10.1039/c4ce01169d.

[21] G. Zhou, X. Xu, T. Ding, B. Feng, Z. Bao, J. Hu, Well-steered charge-carrier transfer in 3D branched Cu$_x$O/ZnO@Au heterostructures for efficient photocatalytic hydrogen evolution, ACS Appl. Mater. Interfaces 7 (2015) 26819–26827, https://doi.org/10.1021/acsami.5b09027.

[22] D. Chen, J. Liu, Z. Jia, J. Fang, F. Yang, Y. Tang, K. Wu, Z. Liu, Z. Fang, Efficient visible-light-driven hydrogen evolution and Cr(VI) reduction over porous P and Mo co-doped g-C$_3$N$_4$ with feeble N vacancies photocatalyst, J. Hazard. Mater. 361 (2019) 294–304, https://doi.org/10.1016/j.jhazmat.2018.09.006.

[23] Z. Lv, H. Zhou, H. Liu, B. Liu, M. Liang, H. Guo, Controlled assemble of oxygen vacant CeO$_2$@ Bi$_2$WO$_6$ hollow magnetic microcapsule heterostructures for visible-light photocatalytic activity, Chem. Eng. J. 330 (2017) 1297–1305, https://doi.org/10.1016/j.cej.2017.08.074.

[24] G. Zhou, Y. Hu, L. Long, P. Wang, Y. Shan, L. Wang, J. Guo, C. Zhang, Y. Zhang, L. Liu, Charged excited state induced by ultrathin nanotip drives highly efficient hydrogen evolution, Appl. Catal. B: Environ. 262 (2020), https://doi.org/10.1016/j.apcatb.2019.118305, 118305.

[25] Y. Wang, L. Rao, P. Wang, Z. Shi, L. Zhang, Photocatalytic activity of N-TiO$_2$/O-doped N vacancy g-C$_3$N$_4$ and the intermediates toxicity evaluation under tetracycline hydrochloride and Cr(VI) coexistence environment, Appl. Catal. B: Environ. 262 (2020), https://doi.org/10.1016/j.apcatb.2019.118308, 118308.

[26] X. Niu, G. Wu, X. Zhang, J. Wang, Interlayer coupling prolonged the photogenerated carrier lifetime of few layered Bi$_2$OS$_2$ semiconductors, Nanoscale 12 (2020) 6057–6063, https://doi.org/10.1039/D0NR00447B.

[27] G. Zhou, Z. Guo, Y. Shan, S. Wu, J. Zhang, K. Yan, L. Liu, P.K. Chu, X. Wu, High-efficiency hydrogen evolution from seawater using hetero-structured T/Td phase ReS$_2$ nanosheets with cationic vacancies, Nano Energy 55 (2019) 42–48, https://doi.org/10.1016/j.nanoen.2018.10.047.

[28] C. Clavero, Plasmon-induced hot-electron generation at nanoparticle/metal-oxide interfaces for photovoltaic and photocatalytic devices, Nat. Photonics 8 (2014) 95, https://doi.org/10.1038/nphoton.2013.238.

[29] R. Mu, Y. Ao, T. Wu, C. Wang, P. Wang, Synthesis of novel ternary heterogeneous anatase-TiO$_2$ (B) biphase nanowires/Bi$_4$O$_5$I$_2$ composite photocatalysts for the highly efficient degradation of acetaminophen under visible light irradiation, J. Hazard. Mater. 382 (2020), https://doi.org/10.1016/j.jhazmat.2019.121083, 121083.

[30] G. Zhou, Y. Shan, Y. Hu, X. Xu, L. Long, J. Zhang, J. Dai, J. Guo, J. Shen, S. Li, L. Liu, X. Wu, Half-metallic carbon nitride nanosheets with micro grid mode resonance structure for efficient photocatalytic hydrogen evolution, Nat. Commun. 9 (2018) 3366, https://doi.org/10.1038/s41467-018-05590-x.

[31] G. Zhou, Y. Shan, L. Wang, Y. Hu, J. Guo, F. Hu, J. Shen, Y. Gu, J. Cui, L. Liu, X. Wu, Photoinduced semiconductor-metal transition in ultrathin troilite FeS nanosheets to trigger efficient hydrogen evolution, Nat. Commun. 10 (2019) 1–8, https://doi.org/10.1038/s41467-019-08358-z.

[32] X. Niu, Y. Li, Y. Zhang, Q. Zheng, J. Zhao, J. Wang, Highly efficient photogenerated electron transfer at a black phosphorus/Indium selenide heterostructure interface from ultrafast dynamics, J. Mater. Chem. C 7 (2019) 1864–1870, https://doi.org/10.1039/C8TC06208K.

[33] Q.H. Wang, K. Kalantar-Zadeh, A. Kis, J.N. Coleman, M.S. Strano, Electronics and optoelectronics of two-dimensional transition metal dichalcogenides, Nat. Nanotechnol. 7 (2012) 699–712, https://doi.org/10.1038/nnano.2012.193.

[34] D.Y. Qiu, F.H. Jornada, S.G. Louie, Optical spectrum of MoS$_2$: many-body effects and diversity of exciton states, Phys. Rev. Lett. 111 (2013), https://doi.org/10.1103/PhysRevLett.111.216805, 216805.

[35] Y. Zhang, T.R. Chang, B. Zhou, Y.T. Cui, H. Yan, Z. Liu, F. Schmitt, J. Lee, R. Moore, Y. Chen, H. Lin, H.T. Jeng, S.K. Mo, Z. Hussain, A. Bansil, Z.X. Shen, Direct observation of the transition of indirect to direct bandgap in atomically thin epitaxial MoSe$_2$, Nat. Nanotechnol. 9 (2014) 111–115, https://doi.org/10.1038/nnano.2013.277.

[36] S. Tongay, H. Sahin, C. Ko, A. Luce, W. Fan, K. Liu, J. Zhou, Y.S. Huang, C.H. Ho, J. Yan, D.F. Ogletree, S. Aloni, J. Li, S. Li, J. Li, F.M. Peeters, J. Wu, Monolayer behavior in bulk ReS$_2$ due to electronic and vibrational decoupling, Nat. Commun. 5 (2014) 3252, https://doi.org/10.1038/ncomms4252.

[37] Y. Fu, Y. Shan, G. Zhou, L. Long, L. Wang, K. Yin, J. Guo, J. Shen, L. Liu, X. Wu, Electric strain in dual metal Janus nanosheets induces structural phase transition for efficient hydrogen evolution, Joule 3 (2019) 2955–2967, https://doi.org/10.1016/j.joule.2019.09.006.

[38] Y. Fu, T. Li, G. Zhou, J. Guo, Y. Ao, Y. Hu, J. Shen, L. Liu, X. Wu, Dual-metal-driven selective pathway of nitrogen reduction in orderly atomic-hybridized Re$_2$MnS$_6$ ultrathin nanosheets, Nano Lett. 20 (2020) 4960–4967, https://doi.org/10.1021/acs.nanolett.0c01037.

[39] X. Zhou, J. Lan, G. L, K. Deng, Y. Yang, G. Nie, J. Yu, L. Zhi, Facet-mediated photodegradation of organic dye over hematite architectures by visible light, Angew. Chem. Int. Ed. 51 (2012) 178–182, https://doi.org/10.1002/anie.201105028.

[40] J.P. Perdew, K. Buke, M. Ernzerhof, Generalized gradient approximation made simple, Phys. Rev. Lett. 77 (1996) 3865–3868, https://doi.org/10.1103/PhysRevLett.77.3865.

[41] F. Ricci, E. Bousquet, Unveiling the room-temperature magnetolectricity of troilite FeS, Phys. Rev. Lett. 116 (2017) 227601–227605, https://doi.org/10.1103/PhysRevLett.116.227601.

[42] X. Li, S. Zhang, S.A. Kulinich, Y. Liu, H. Zeng, Engineering surface states of carbon dots to achieve controllable luminescence for solid-luminescent composites and sensitive Be$^{2+}$ detection, Sci. Rep. 4 (2014) 4976, https://doi.org/10.1038/srep04976.

[43] B. Yuan, S. Guan, X. Sun, X. Li, H. Zeng, Z. Xie, P. Chen, S. Zhou, Highly efficient carbon dots with reversibly switchable green-red emissions for trichromatic white light-emitting diodes, ACS Appl. Mater. Interfaces 10 (2018) 16005–16014, https://doi.org/10.1021/acsami.8b02379.

[44] F. Yuan, Z. Wang, X. Li, Y. Li, Za Tan, L. Fan, S. Yang, Bright multicolor bandgap fluorescent carbon quantum dots for electroluminescent light-emitting diodes, Adv. Mater. 29 (2017), https://doi.org/10.1002/adma.201604436, 1604436.

[45] X. Wang, L. Cao, F. Lu, M.J. Meziani, H. Li, G. Qi, B. Zhou, B.A. Harruff, F. Kermarrec, Y.P. Sun, Photoinduced electron transfers with carbon dots, Chem. Commun. 25 (2009) 3774–3776, https://doi.org/10.1039/B906252A.

[46] P. Zhang, T. Song, T. Wang, H. Zeng, In-situ synthesis of Cu nanoparticles hybridized with carbon quantum dots as a broad spectrum photocatalyst for improvement of photocatalytic H$_2$ evolution, Appl. Catal. B: Environ. 206 (2017) 328–335, https://doi.org/10.1016/j.apcatb.2017.01.051.

[47] S. Zhu, J. Zhang, S. Tang, C. Qiao, L. Wang, H. Wang, X. Liu, B. Li, Y. Li, W. Yu, X. Wang, H. Sun, B. Yang, Surface chemistry routes to modulate the photoluminescence of graphene quantum dots: from fluorescence mechanism to up conversion bioimaging applications, Adv. Funct. Mater. 22 (2012) 4732–4740, https://doi.org/10.1002/adfm.201201499.

[48] M. Li, S.K. Cushing, X. Zhou, S. Guo, N. Wu, Fingerprinting photoluminescence of functional groups in graphene oxide, J. Mater. Chem. 22 (2012) 23374–23379, https://doi.org/10.1039/C2JM35417A.

[49] X.L. Wu, S.J. Xiong, Z. Liu, J. Chen, J.C. Shen, T.H. Li, P.H. Wu, P.K. Chu, Green light stimulates terahertz emission from mesocrystal microspheres, Nat. Nanotechnol. 6 (2012) 103–106, https://doi.org/10.1038/nnano.2010.264.

[50] J. Wang, S.J. Xiong, X.L. Wu, T.H. Li, P.K. Chu, Glycerol-bonded 3C-SiC nanocrystal solid films exhibiting broad and stable violet to blue-green emission, Nano Lett. 10 (2010) 1466–1471, https://doi.org/10.1021/nl100407d.

[51] X.L. Wu, Y.F. Mei, G.G. Siu, K.L. Wong, K. Moulding, M.J. Stokes, C.L. Fu, X.M. Bao, Spherical growth and surface-quasifree vibrations of Si nanocrystallites in Er-doped Si nanostructures, Phys. Rev. Lett. 86 (2001) 3000–3003, https://doi.org/10.1103/PhysRevLett.86.3000.

[52] X.L. Wu, S.J. Xiong, G.G. Siu, G.S. Huang, Y.F. Mei, Z.Y. Zhang, S.S. Deng, C. Tan, Optical emission from excess Si defect centers in Si nanostructures, Phys. Rev. Lett. 91 (2003), https://doi.org/10.1103/PhysRevLett.91.157402, 157402.

[53] P.Q. Zhao, Q.Z. Zhang, X.L. Wu, Interaction between water molecules and 3C-SiC nanocrystal surface, Sci. China - Phys. Mech. Astron. 57 (2014) 819–828, https://doi.org/10.1007/s11433-014-5442-0.

[54] L.Z. Liu, J.Q. Xu, X.L. Wu, T.H. Li, J.C. Shen, P.K. Chu, Optical identification of oxygen vacancy types in SnO$_2$ nanocrystals, Appl. Phys. Lett. 102 (2013), 031916, https://doi.org/10.1063/1.4789538.

[55] I. Concina, Z.H. Ibupoto, A. Vomiero, Semiconducting metal oxide nanostructures for water splitting and photovoltaics, Adv. Energy Mater. 7 (2017), https://doi.org/10.1002/aenm.201700706, 1700706.

[56] Y. Yang, S. Niu, D. Han, T. Liu, G. Wang, Y. Li, Progress in developing metal oxide nanomaterials for photoelectrochemical water splitting, Adv. Energy Mater. 7 (2017), https://doi.org/10.1002/aenm.201700555, 1700555.

[57] Z. Hong, B. Shen, Y. Chen, B. Lin, B. Gao, Enhancement of photocatalytic H$_2$ evolution over nitrogen-deficient graphitic carbon nitride, J. Mater. Chem. A 1 (2013) 11754–11761, https://doi.org/10.1039/C3TA12332D.